=========== **SOLID STATE** ===========

Structure and Thermoelastic Martensitic Transformations in Ternary Ni–Ti–Hf Alloys with a High-Temperature Shape Memory Effect

V. G. Pushin*[a,b], N. N. Kuranova[a], A. V. Pushin[a,b], A. N. Uksusnikov[a], and N. I. Kourov[a]

[a] *Institute of Metal Physics, Ural Branch, Russian Academy of Sciences,
ul. S. Kovalevskoi 18, Yekaterinburg, 620990 Russia*
[b] *Ural Federal University, ul. Mira 19, Yekaterinburg, 620002 Russia*
*e-mail: pushin@imp.uran.ru
Received September 30, 2015

Abstract—The effect of alloying by 12–20 at % Hf on the structure, the phase composition, and the thermoelastic martensitic transformations in ternary alloys of the quasi-binary NiTi–NiHf section is studied by transmission electron microscopy, scanning electron microscopy, electron diffraction, and X-ray diffraction. The electrical resistivity is measured at various temperatures to determine the critical transformation temperatures. The data on phase composition are used to plot a full diagram for the high-temperature thermoelastic $B2 \leftrightarrow B19'$ martensitic transformations, which occur in the temperature range 320–600 K when the hafnium content increases from 12 to 20 at %. The lattice parameters of the $B2$ and $B19'$ phases are measured, and the microstructure of the $B19'$ martensite is analyzed.

INTRODUCTION

Binary titanium nickelide alloys are known to have the best set of physicochemical properties among the metallic materials exhibiting thermoelastic martensitic transformations (TMTs) and the shape memory effect (SME) that have been developed to date [1–6]. Nevertheless, even the application of these alloys in a standard polycrystalline state not always ensures the required physicomechanical parameters. Alloys with high-temperature TMTs and SME have recently attracted particular attention of researchers [4–22]. It is known that elements such as Pd, Au, and Pt (which are $B2$ stabilizers at a high content), substitute for nickel atoms in $Ti_{50}Ni_{50}$ alloys and substantially increase the $B2 \leftrightarrow B19$ transformation temperatures. In contrast, they decrease the $B2 \leftrightarrow B19'$ transformation temperatures at a low content. At intermediate contents, they cause sequential $B2 \leftrightarrow B19 \leftrightarrow B19'$ TMTs [4, 5]. When titanium nickelide is alloyed with copper, qualitatively similar changes in the type and sequence of TMTs occur. Nevertheless, their critical temperatures could not be substantially increased as compared to the TMT temperatures in binary equiatomic titanium nickelide [2, 5]. The substitution of hafnium for titanium atoms from 10 to 30 at % increases the $B2 \leftrightarrow B19'$ TMT temperature up to 800 K [7, 13]. However, the $B2$-superstructure-based solid solution could not be retained in alloys with a nickel content near 50 at %; as a result, a number of excess phases can form [7, 13, 14, 16]. For example, $Ni_4(Ti,Hf)_3$ particles precipitate in the alloys with more than 50 at % Ni [16], and $(Ti,Hf)_2Ni$-type phase precipitates in the alloys with less than 50 at % Ni during high-temperature heat treatment at, e.g., 973 K [14]. Obviously, the decomposition of $B2$-based Ni–Ti–Hf solid solutions would result in a substantial change in the critical TMT temperatures and the properties of the alloys.

Thus, the TMTs and the physicomechanical properties of the alloys depend strongly on the hafnium concentration and the precision of alloying and, if necessary, heat treatment, which retain stoichiometric quasi-binary substitution of hafnium for only titanium atoms and prevent decomposition. In particular, the excess phases that form in nonstoichiometric ternary Ni–Ti–Hf alloys can be one of the key causes of their low plasticity. The decomposition of the $B2$ phase precedes the formation of monoclinic $B19'$ martensite crystals (as in the case of martensite in binary Ti–Ni alloys); as a result, the SME parameters and other structural and functional characteristics of the alloys are known to change. The data on the key characteristics of TMTs and the physicomechanical properties of the alloys that are close to quasi-binary NiTi–NiHf compositions are still different and conflicting [7–22]. The purpose of this work is to comprehensively study ternary $Ni_{50}Ti_{50-x}Hf_x$ ($12 \leqslant x \leqslant 20$ at %) alloys with a precision chemical composition in nickel, titanium, and hafnium.
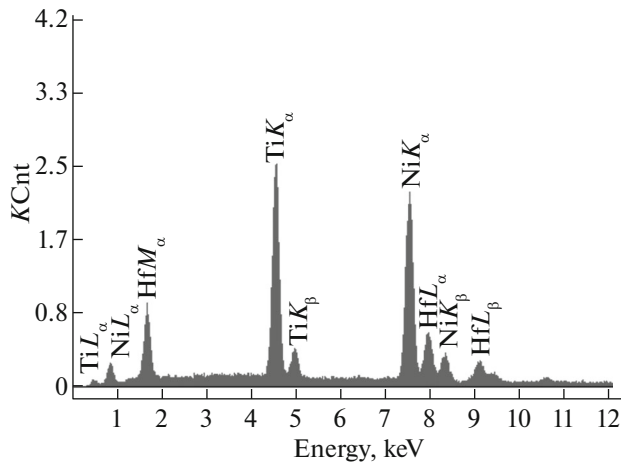
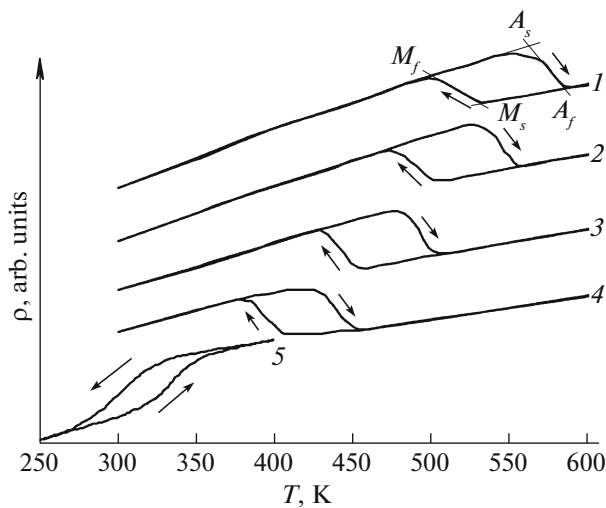**Fig. 1.** Typical characteristic X-ray spectrum of the $Ni_{50}Ti_{38}Hf_{12}$ alloy.

Fig. 2. Fragment of the X-ray diffraction pattern of $Ni_{50}Ti_{38}Hf_{12}$.

Fig. 3. Temperature dependences of the electrical resistivity of $Ni_{50}Ti_{50-x}Hf_x$ alloys: (*1*) 20, (*2*) 18, (*3*) 15, (*4*) 12, and (*5*) 0 at % Hf.
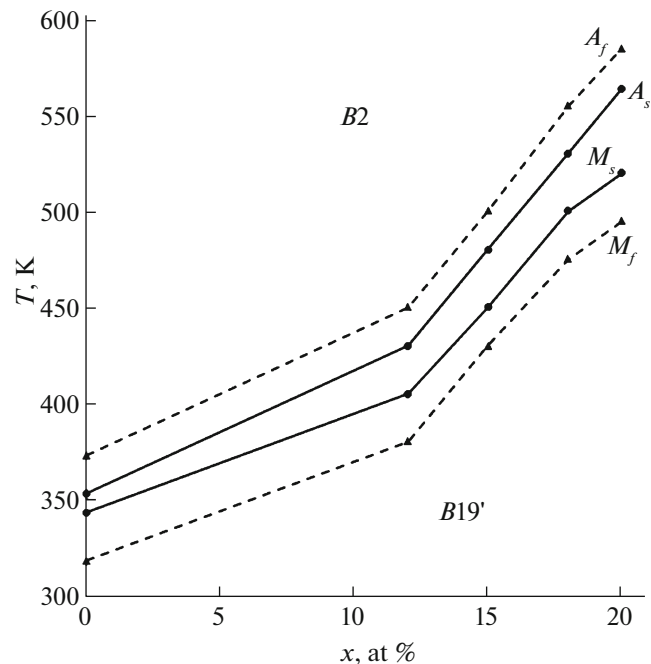
Fig. 4. Diagram of the $B2 \leftrightarrow B19'$ TMT in $Ni_{50}Ti_{50-x}Hf_x$ ($0 \leqslant x \leqslant 20$) alloys.

EXPERIMENTAL

The alloys to be studied were prepared by electric arc melting from high-purity Ni and Cu (99.99%), Ti (99.8%), and Hf (99.9%) in a purified helium atmosphere. The alloys preliminarily selected according to chemical composition were subjected to remelting at least three times for homogenization, subsequent hot upsetting by 5−10% in a press, long-term annealing at 1073 K in argon, and quenching. As a result, we achieved a substantially more uniform grain size distribution (50−70 μm) and a chemical composition distribution as compared to the corresponding as-cast prototype alloys and were able to exclude segregation after casting. For investigations, we chose alloys with 49.5−49.7 at % Ni. The structure and the phase transformations in the alloys quenched from 1073 K
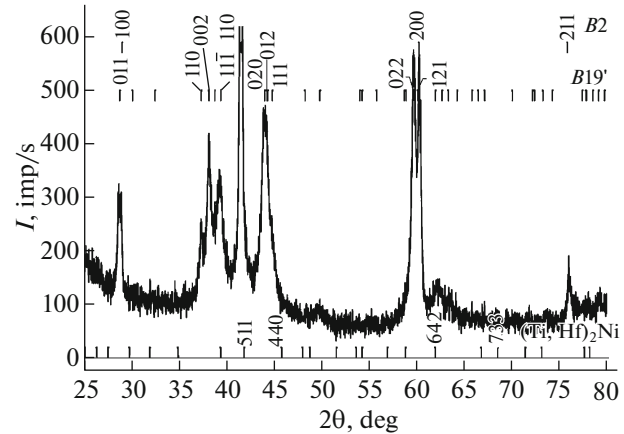
were analyzed by X-ray diffraction (XRD), transmission electron microscopy (TEM), and scanning electron microscopy (SEM), including in situ experiments upon heating and cooling. XRD θ/2θ analysis was performed on a DRON-3M diffractometer using CuK_α radiation monochromatized by a graphite single crystal. Electron-microscopic investigations were carried out on JEM-200 CX (maximum accelerating voltage of 200 kV) and Tecnai G^2 30 (maximum accelerating voltage of 300 kV) microscopes and a Quanta 200 (accelerating voltage up to 30 kV) scanning electron microscope equipped with the Pegasus (EDS, EBSD) system, which are located at the Nanotechnology and
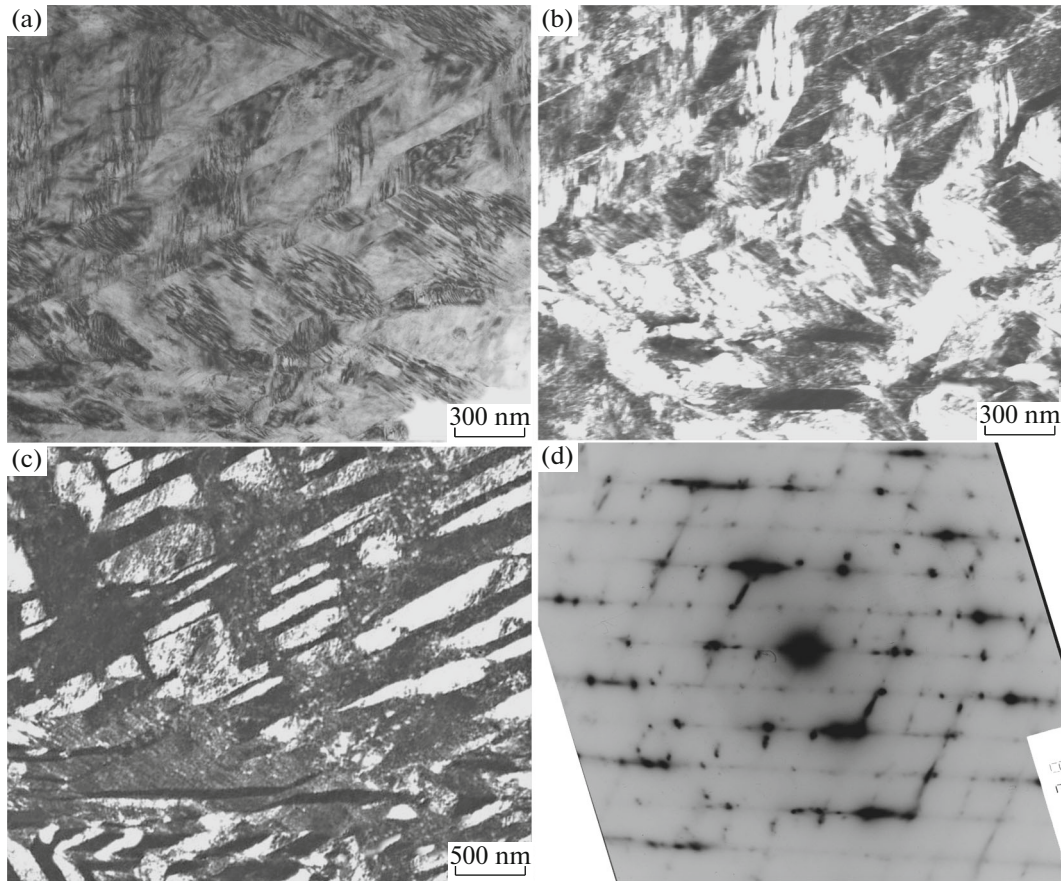
Fig. 5. (a) Bright-field and (b, c) dark-field TEM images and (d) corresponding electron diffraction pattern of the $Ni_{50}Ti_{32}Hf_{18}$ alloy.

Advanced Materials Testing Center for Collective Use, Institute of Metal Physics. The electrical resistivities of the alloys were measured over a wide temperature range.

RESULTS AND DISCUSSION

The chemical compositions of all alloys were determined by the EDAX energy dispersive spectrometer attached to Quanta Pegasus SEM. Figure 1 shows the typical characteristic X-ray spectrum of the alloy with the nominal composition $Ni_{50}Ti_{38}Hf_{12}$; according to the energy dispersive microanalysis data, it contains 49.52 at % Ni, 38.14 at % Ti, and 12.34 at % Hf. As noted above, for a comprehensive investigation we chose the alloys with 49.5–49.7 at % Ni to avoid the influence of low-temperature decomposition accompanied by the precipitation nickel-rich phases on the TMT characteristics and, on the other hand, to study the alloys that are as close to stoichiometry as possible with allowance for the high-temperature formation of Ti_2Ni-type phases enriched in titanium and, apparently, hafnium and oxygen [11].

The XRD data demonstrate that all alloys are in a predominant martensitic state at room temperature.

Critical $B2 \leftrightarrow B19'$ TMT temperatures of quasi-binary $Ni_{50}Ti_{50-x}Hf_x$ alloys

Alloy	M_s, K	M_f, K	A_s, K	A_f, K	ΔM	ΔA	(A_f-M_s)	(A_s-M_f)	(A_f-M_f)	(A_s-M_s)
$Ni_{50}Ti_{50}$	343	318	353	373	25	20	30	35	55	10
$Ni_{50}Ti_{38}Hf_{12}$	405	380	430	450	25	20	45	50	70	25
$Ni_{50}Ti_{35}Hf_{15}$	450	430	480	500	20	20	50	50	70	30
$Ni_{50}Ti_{32}Hf_{18}$	500	475	530	555	25	25	55	55	80	30
$Ni_{50}Ti_{30}Hf_{20}$	520	495	564	585	25	20	65	70	90	45
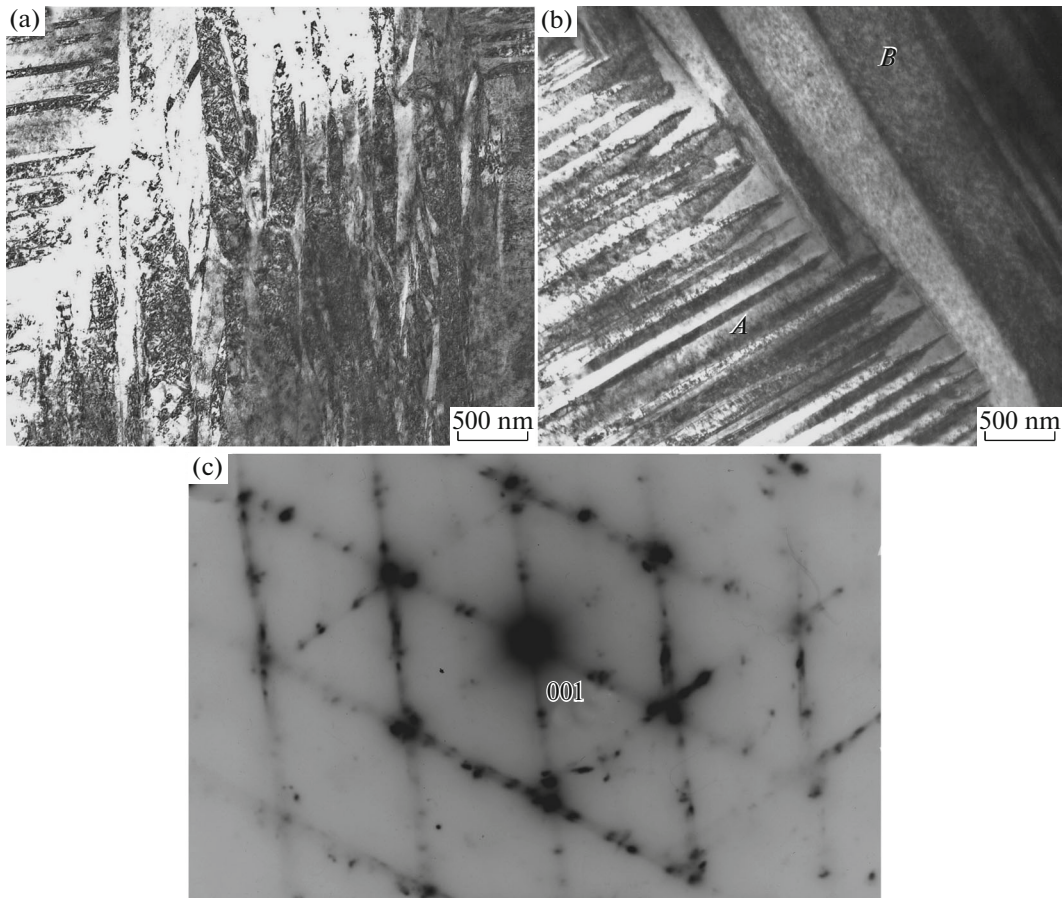
Fig. 6. (a, b) Bright-field TEM images and (c) corresponding electron diffraction pattern of (a) $Ni_{50}Ti_{35}Hf_{15}$ and (b, c) $Ni_{50}Ti_{30}Hf_{20}$ alloys. (*A*, *B*) Junctions of two packets.

XRD was used to determine the phase compositions of the alloys and to measure the parameters of the *B*2 austenite and the *B*19' martensite in them. Figure 2 shows the typical X-ray diffraction pattern of one of the alloys and the bar X-ray diffraction patterns of the detected phases. It was found that the *B*2 austenite parameters increased from 0.3015 to 0.3090 nm upon alloying with 0−20 at % Hf. The *B*19' martensite parameters also grow in this case. The *B*19' lattice parameters in the $Ti_{50}Ni_{50}$ are $a_{B19'} = 0.289-0.291$ nm, $b_{B19'} = 0.412-0.411$ nm, $c_{B19'} = 0.464-0.466$ nm, and $\beta = 96.8°-97.8°$ [15]. In the alloys with 0−20 at % Hf, they change in the ranges $a_{B19'} = 0.301-0.302$ nm, $b_{B19'} = 0.410-0.408$ nm, $c_{B19'} = 0.480-0.485$ nm, and $\beta = 99.3°-102.8°$, which agrees with the well-known experimental and theoretical data for ternary alloys with 12, 15, 18, and 20 at % Hf [9, 11, 14, 16, 17]. Moreover, X-ray diffraction patterns always exhibited weak effects of an excess $(Ti,Hf)_2Ni$ phase with a lattice parameter $a_{(Ti,Hf)2Ni} = 1.120$ nm.

Based on an analysis of the chemical compositions of the alloys and the almost linear relation between the *B*19' lattice parameters and the hafnium content, we can conclude that the near-stoichiometric Ni−Ti−Hf alloys are substitutional solid solutions. One of the *B*2-superstructure sublattices is statistically filled with titanium and hafnium atoms with close radii, and the other sublattice is filled with nickel atoms.

The following three temperature measurement methods are usually applied to determine the critical temperatures of the onset (M_s, A_s) and end (M_f, A_f) of the forward (M_s, M_f) and reverse (A_s, A_f) TMTs: electrical resistivity $\rho(T)$ measurements, magnetic susceptibility $\chi(T)$ measurements, and differential scanning calorimetry (DSC) [1−6]. We measured $\rho(T)$ curves upon heating and cooling for all alloys that exhibit temperature $\rho(T)$ loops corresponding to the temperature TMT hystereses (Fig. 3). The critical TMT temperatures were determined from the $\rho(T)$ curves by drawing two tangents. These temperatures are given in the table and were used to plot TMT diagrams of the alloys (Fig. 4). An analysis showed that all temperatures of the $B2 \leftrightarrow B19'$ TMT increase almost identically upon alloying in the range 12−20 at % Hf.

The obtained critical TMT temperatures of the alloys can be used to find the temperature characteris-
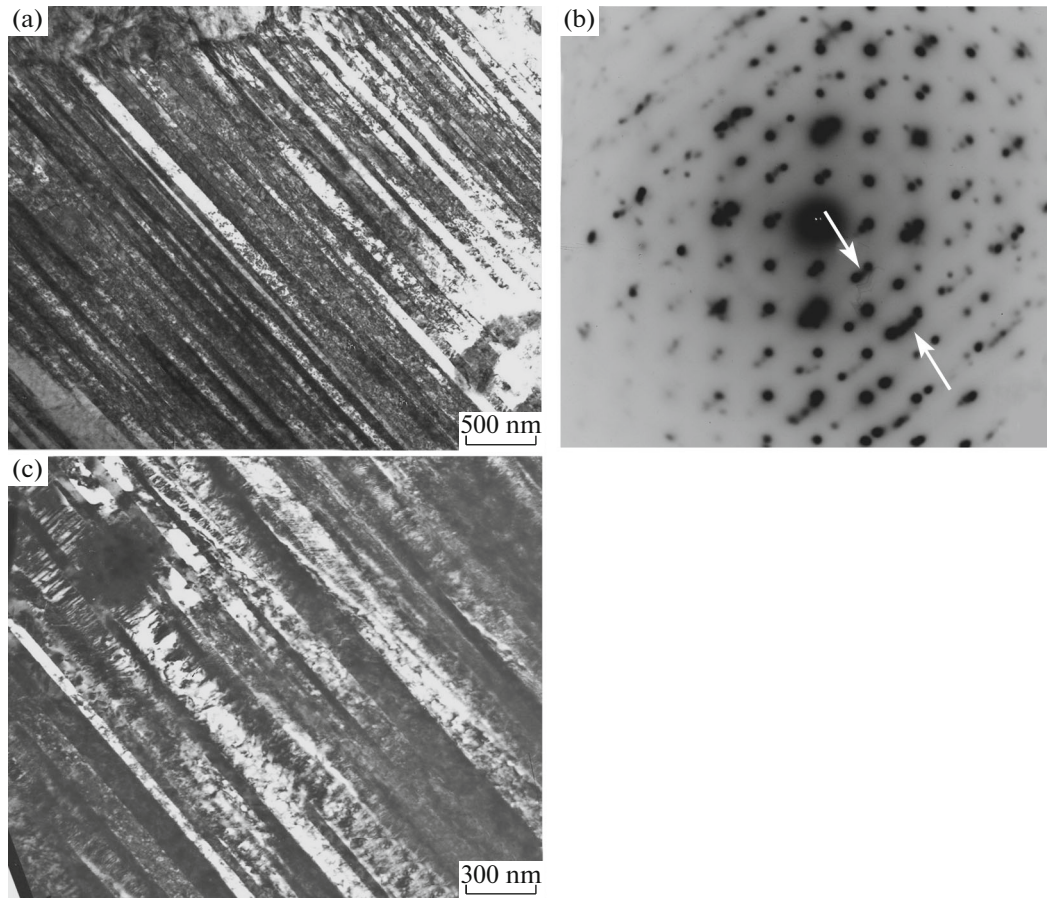
Fig. 7. (a) Bright-field and (c) dark-field TEM images and (b) corresponding electron diffraction pattern of the $Ni_{50}Ti_{38}Hf_{12}$ alloy. One-packet morphology. Weak reflections of the $B2$ austenite are indicated by the arrows.

tics of the TMT hysteresis in various alloys (table). Note that the hysteresis of the alloys studied in [18] turned out to be twice as large as the hysteresis of the deformed and recrystallized alloys studied in this work, which is likely to be related to segregation heterogeneity and different grain sizes in the as-cast alloys analyzed in [18]. The binary $Ni_{50}Ti_{50}$ alloy has the narrowest hysteresis.

The electron-microscopic examination of the microstructure of the quasi-binary alloys showed the following. Their microstructure is characterized by a predominantly packet morphology of martensite crystals (Figs. 5−7). The packet morphology of $B19'$ crystals with thin secondary twins along the $\{011\}\langle 00\bar{1}\rangle$ shear system is most pronounced in the alloys with crystals having zone axes (ZAs) $[100]_{B19'} \parallel [100]_{B19'}^{tw} \parallel [100]_{B2}$ (see Fig. 7). Note that the weak reflections of retained $B2$ austenite, such as 100_{B2} and 200_{B2}, are most reliably revealed in this case (Fig. 7b).

In another typical example of one- or two-packet morphology of martensite (where ZAs are close to $[110]_{B19'} \parallel [111]_{B2}$), parallel crystals of the initial orien-

tation alternate with I-type microtwins along $(1\bar{1}1)_{B19'}$ (Figs. 5, 6). Thin secondary composite nanotwins along $(001)_{B19'}$ are also present inside them (Figs. 5a, 5b). They manifest themselves in electron diffraction patterns as sharp streaks along the $[001]_{B19'}$ directions in the reciprocal lattice (Figs. 5d, 6c). $(001)_{B19'}$ nanotwins are located at a certain angle to twin boundaries in packets and are also visible in a dark-field image (Fig. 7c). As follows from an analysis of electron diffraction patterns, the orientation relationships of martensite $B19'$ crystals are close to the Bain orientation relationships $(100)_{B2} \parallel (100)_{B19'}$, $[011]_{B2} \parallel [010]_{B19'}$, and $[0\bar{1}1]_{B2} \parallel [011]_{B19'}$.

According to phenomenological crystallographic theories [21], $\langle 011 \rangle$ twinning mode II, which is responsible for invariant lattice shear during the $B2 \leftrightarrow B19'$ TMT, dominates in the substructure of the $B19'$ substructure in binary titanium nickelide $Ti_{50}Ni_{50}$. However, $B19'$ martensite in the hafnium-containing alloys is characterized by predominant (011) and $(1\bar{1}1)_{B19'}$ twins of type I and composite twins along $(001)_{B19'}$ and has no twins of type II [8, 9, 11, 19, 21]. Generally

speaking, the I-type twins can also provide the geo-metrically necessary shear with an invariant lattice during the $B2 \leftrightarrow B19'$ TMT in these alloys. The composite twins along $(001)_{B19'}$ are assumed to have a deformation−accommodation origin.

CONCLUSIONS

The following results were obtained. The critical temperatures were measured and generalized full diagrams were plotted for the $B2 \leftrightarrow B19'$ TMTs in polycrystalline quasi-binary NiTi−NiHf alloys with a hafnium content up to 20 at %. At room temperature, along with a predominant martensite phase, the quenched alloys have a certain content of retained $B2$ austenite and an intermetallic $(Ti,Hf)_2Ni$-type phase. The lattice parameters of the $B19'$, $B2$, and $(Ti,Hf)_2Ni$ phases were determined. The structure of the $B19'$ martensite phase is characterized by a packet morphology of pair-twinned thin lamellar crystals with predominant (011) and $(1\bar{1}1)_{B19'}$ twins of type I. The martensite crystals contain composite twins and $(001)_{B19'}$ stacking faults, which are characteristic of the $B19'$ martensite in all titanium nickelide alloys.

ACKNOWLEDGMENTS

REFERENCES

1. V. A. Likhachev, S. L. Kuz'min, and Z. P. Kamentseva, *Shape-Memory Effect* (Leningrad State Univ., Leningrad, 1987).

2. K. Ootsuka, K. Simidzu, Yu. Sudzuki, et al., *Alloys with Shape-Memory Effect* (Metallurgiya, Moscow, 1990).

3. V. N. Khachin, V. G. Pushin, and V. V. Kondrat'ev, *Titanium Nickelide: Structure and Properties* (Nauka, Moscow, 1992).

4. V. G. Pushin, V. V. Kondrat'ev, and V. N. Khachin, *Pretransitional Phenomena and Martensitic Transforma-tions* (Ural Otd. Ross. Akad. Nauk, Yekaterinburg, 1998).

5. V. G. Pushin, S. D. Prokoshkin, R. Z. Valiev, et al., *Nickelide Titanium alloys with Shape-Memory Effect*, Part 1: *Structure, Phase Transitions, and Properties* (Ural Otd. Ross. Akad. Nauk, Yekaterinburg, 2006).

6. V. G. Pushin, Fiz. Met. Metalloved. **90**, Suppl. 1, 568 (2000).

7. D. Agunst, P. Thoma, and M. Kao, J. Phys. IV, Colloq. **C8**, 747 (1995).

8. X. D. Han, W. H. Zou, R. Wang, Z. Zhang, and D. Z. Yang, Acta Mater. **44**, 3711 (1996).

9. X. D. Han, R. Wang, Z. Zhang, and D. Z. Yang, Acta Mater. **46**, 273 (1998).

10. S. F. Hsieh and S. K. Wu, Mater. Charact. **41**, 151 (1998).

11. Y. F. Zheng, W. Cai, J. X. Zhang, Y. Q. Wang, L. C. Zhao, and H. Q. Ye, Mater. Lett. **36**, 142 (1998).

12. K. Otsuka and X. Ren, Prog. Mater. Sci. **7**, 511 (1999).

13. S. Besseghini, E. Villa, and A. Tuissi, Mater. Sci Eng. A **273−275**, 390 (1999).

14. X. L. Meng, Y. F. Zheng, Z. Wang, and L. C. Zhao, Scr. Mater. **42**, 341 (2000).

15. C. S. Firstov, J. Van Humbeeck, and Yu. N. Koval, Scr. Mater. **50**, 243 (2004).

16. X. L. Meng, W. Cai, F. Chen, and L. C. Zhao, Scr. Mater. **54**, 1599 (2006).

17. S. L. Tan, W. Cai, and X. H. Tian, Chin. Phys. **15**, 2718 (2006).

18. V. Kolomytsev, M. Babanky, A. Pasko, et al., Adv. Sci. Technol. **59**, 113 (2008).

19. X. L. Meng, Y. D. Fu, W. Cai, Q. F. Li, and L. C. Zhao, Philos. Mag. Lett. **89**, 431 (2009).

20. C. M. Denowh and D. A. Miller, Smart Mater. Struct. **21**, 065 020 (2012).

21. A. Evirgen, I. Karaman, H. E. Karaea, and R. D. Noebe, Acta Mater. **61**, 6191 (2013).

22. T. E. Kuntsevich, A. V. Pushin, and V. G. Pushin, Tech. Phys. Lett. **40**, 449 (2014).

Translated by K. Shakhlevich